

UC Davis

UC Davis Electronic Theses and Dissertations

Title

Molten Hydroxide Flux Synthesis of KNi₄S₂ and its Magnetic and Physical Properties

Permalink

<https://escholarship.org/uc/item/9vg7j8sd>

Author

Cardenas, Edward

Publication Date

2023

Peer reviewed|Thesis/dissertation

Molten Hydroxide Flux Synthesis of KNi_4S_2 and its Magnetic and Physical Properties

By

EDWARD ALLYN CARDENAS

THESIS

Submitted in partial satisfaction of the requirements for the degree of

MASTER OF SCIENCE

in

Chemistry

in the

OFFICE OF GRADUATE STUDIES

of the

UNIVERSITY OF CALIFORNIA

DAVIS

Approved:

Valentin Taufour, Chair

Susan Kauzlarich

Jesús Velázquez

Committee in Charge

2023

CONTENTS

List of Figures	iii
List of Tables	iii
I. Abstract	iv
II. Introduction	1
III. Experimental Methods	4
A. Single Crystal Synthesis	4
B. Powder X-Ray Diffraction	8
C. Magnetic Characterization	8
D. Resistivity	10
E. Heat Capacity	11
IV. Results and Discussion	13
A. KNi_4S_2	13
1. Synthesis	13
2. Magnetization Data	14
3. Resistivity	18
4. Heat Capacity	19
B. KNi_2S_2	21
1. Introduction	21
2. XRD	22
3. Magnetization Data	23
C. $\text{K}_2\text{Ni}_3\text{S}_4$	24
1. Introduction	24
2. Magnetization Data	26
V. Future Work	26
A. Potential Dopings	26
B. Pressure Studies	27
VI. Conclusion	28
Acknowledgments	28
A. Table of Synthesis Notes	29
B. MPMS Goodness of Fit	29
References	32

LIST OF FIGURES

1	Synthesis Phase diagram	4
2	Temperature Profile for KNi_4S_2	5
3	KOH-LiOH Phase Diagram	5
4	KNi_4S_2 Crystals Before and After	6
5	Temperature Profile for KNi_2S_2	7
6	Temperature Profile for the $\text{K}_2\text{Ni}_3\text{S}_4$	7
7	KNi_4S_2 Mosaic for MPMS measurements	9
8	KNi_4S_2 Wired for Resistivity	10
9	KNi_4S_2 Intro	13
10	KNi_4S_2 samples without twinning	14
11	KNi_4S_2 Polycrystalline M v. T	15
12	KNi_4S_2 Single Crystal Mosaic M v. T	16
13	KNi_4S_2 Polycrystalline M v. H	16
14	KNi_4S_2 Pellet M v. T and M v. H	17
15	KNi_4S_2 Single Crystal Mosaic M v. H	17
16	KNi_4S_2 Single Crystal Mosaic M v. H at Room Temperature	19
17	KNi_4S_2 Single Crystal Resistivity	20
18	KNi_4S_2 Heat Capacity	20
19	KNi_2S_2 Introduction	21
20	KNi_2S_2 XRD Phase Confirmation	22
21	KNi_2S_2 Single Crystal M v. T	23
22	$\text{K}_2\text{Ni}_3\text{S}_4$ Introduction	24
23	$\text{K}_2\text{Ni}_3\text{S}_4$ Kagome Lattice	24
24	$\text{K}_2\text{Ni}_3\text{S}_4$ Single Crystal M v. T	25
25	$\text{K}_2\text{Ni}_3\text{S}_4$ Single Crystal M v. H	26
26	KNi_4S_2 Single Crystal Mosaic M v. T Fit	29

LIST OF TABLES

I	Table of Synthesis Notes	30
II	Table of Synthesis Notes Pt. II	31

I. ABSTRACT

This thesis describes how I used the molten-hydroxide flux method of single crystal synthesis to synthesize some of the largest reported single crystals of KNi_4S_2 (142), KNi_2S_2 (122), and $\text{K}_2\text{Ni}_3\text{S}_4$ (234). This molten-hydroxide flux method had previously never been implemented in our lab and, with my optimizations, could open up a previously inaccessible phase-space of meta-stable compounds for our group to explore. I also report the first-known magnetization, resistivity, and heat-capacity data for KNi_4S_2 . Although the KNi_4S_2 phase is isostructural to cuprate superconductors, we do not observe signs of superconductivity nor antiferromagnetic order down to $T = 2$ K. Instead, our magnetization measurements suggest that KNi_4S_2 may be a weak itinerant ferromagnet ($T_C \approx 25$ K). Growing large single crystals allowed us to study magnetic anisotropy, and I found that with KNi_4S_2 , the a and c appear to be isotropic while b seems to be the easy magnetic direction. Resistivity measurements from $T = 1.8 - 300$ K show the 142 phase has a resistivity similar to a bad metal. While I measure a relatively high residual resistivity ratio (RRR) of 44 demonstrating good sample quality, no phase transition is observed in either resistivity or heat capacity measurements. This may be consistent with the weak itinerant nature of the magnetism, although we cannot exclude the possibility of an impurity origin of the ferromagnetic transition. In addition to the 142 phase, I discuss the synthesis and present x-ray diffraction (XRD) patterns and magnetization data for the 122 and 234 phases.

II. INTRODUCTION

Although first observed in 1911 [1], superconductivity’s usefulness in real-world applications was limited by its requirement for impractically low temperatures. Superconductivity is a phase of matter characterized by two main properties: (i) when cooled below a unique critical temperature (T_C), the resistivity vanishes and (ii) the material expels an externally applied magnetic field [2]. Any glimpse into the theory behind this intriguing phenomena was understandably slow to come. In 1957, Bardeen-Cooper-Schrieffer (BCS) theory described a mechanism that explained superconductivity in so-called “conventional” superconductors and reinforced the idea that superconductivity could only occur at low temperatures [3]. Then, Bednorz and Müller, with their discovery of Lanthanum Barium Copper Oxide (LBCO) in 1986, unveiled the first of many “unconventional superconductors” which do not obey BCS theory or any current unifying theory for that matter [4]. In addition to being unconventional, LBCO and many others in its family of copper-oxide-based superconductors known as the cuprates, are also “high critical temperature” (high T_C) materials. High T_C materials are becoming increasingly attractive as the world focuses on more renewable energy resources and faces a global helium shortage. As a result, a significant portion of condensed matter physics research is dedicated to these unconventional superconductors and is driven by an unquenchable thirst for superconductors with higher and higher critical temperatures. There have been many more materials that possess this amazing physical property discovered since: $\text{Ba}_{0.6}\text{K}_{0.4}\text{BiO}_3$ (BKBO) ($T_c \approx 30$ K) in 1988 [5], Cesium-doped fullerenes like Cs_3C_{60} ($T_c \approx 40$ K) known as a class of organic superconductors in 1995 [6], MgB_2 $T_c = 39$ K in 2001 [7] (which is remarkable for being a simple binary with a high T_C , yet has been shown to follow conventional BCS theory), the pnictides [8] or Fe-based superconductors like $\text{SmFeAsO}_{0.85}$ were found to have a $T_c = 55$ K [9] in 2008, and a class of materials that superconduct at high pressures such as H_3S with a $T_c = 203$ K at 90 GPa [10] in 2015 and LaH_{10} with $T_c = 250$ K at 170 GPa just a few years later in 2019 [11].

Although the cuprates are known for having relatively high critical temperatures ($T_c = 98$ K for optimally-doped YBCO [12]), they have limited uses and certain drawbacks associated with them. Such drawbacks are the scalability and shaping of large samples, the mechanical stability when generating large magnetic fields and strain as-

sociated with oxygenation of bulk samples [13]. Recently, a family of materials known as the nickelates have had a renaissance in interest to both experimentalists and theoreticians. They can be isostructural to the cuprates, sharing a square planar molecular geometry between the transition metal site and the chalcogenide as in CaCuO_2 and NdNiO_2 . Both families can be isoelectronic, both Cu(II) and Ni(I) , allow an unusual $3d^9$ electron configuration [14]. The combination of these characteristics are hypothesized to play an important role in the emergence of dome-like superconductivity [15]. After three decades of attempted synthesis and characterization of low-valence nickelates, superconductivity was observed in hole-doped $\text{Nd}_{0.8}\text{Sr}_{0.2}\text{NiO}_2$ thin films synthesized on a SrTiO_3 substrate with a $T_c = 9-15$ K [16]. The phase diagram for $\text{Nd}_{0.8}\text{Sr}_{0.2}\text{NiO}_2$ shows the presence of a superconducting dome in a narrow doping range of $0.125 < x < 0.25$, surrounded by weakly insulating states, which is similar to the cuprates, though these nickelates have a narrower doping window [17]. New questions that arise are the importance of the 4f orbital electrons in these low-valence nickelate systems. For example, LaNiO_2 does not magnetically order nor is it superconducting, but its neodymium counterpart does magnetically order and superconduct [18]. Can we simplify our theory to a “d-only” model just considering the interaction between the 2p orbitals on the chalcogenide and the d^9 electronic configuration of the transition metal [19]? Why is superconductivity only observed in thin film samples of $\text{Nd}_{0.8}\text{Sr}_{0.2}\text{NiO}_2$ and not in bulk samples [20]? This family of materials may give researchers an additional system to investigate the relationship between electronic structure, molecular geometry and superconductivity. However, more compounds of the low-valence nickelates need to be discovered in order to answer these questions. Luckily, another team has made a breakthrough in the difficult synthesis of these materials.

Recently, a team at Argonne National Labs has been able to synthesize single crystals of a new group of nickel chalcogenides [21], which contain nickel in multiple metastable oxidation states. One of the compounds from this new group we intend to explore is KNi_4S_2 . The KNi_4S_2 phase shares the same square planar geometry between the transition metal and the chalcogenide site as the cuprates, along with an electron configuration near monovalent nickel [22]. So far, their synthesis has resulted in small, needle-like single crystals with a maximum length of 1 millimeter, which makes investigation of physical and magnetic properties particularly challenging. The 142 phase

was experimentally synthesized via a molten hydroxide flux method which is not traditionally used in solid state methodology.

Hydroxide fluxes have been used in exploratory synthesis to successfully achieve single crystal samples of various oxides, ceramics, and metallic materials [23]. Their rising popularity is owed to their high thermal stability, low vapor pressure, good electrical conductivity, and their wide useful temperature range [24]. Use of inorganic salts as flux can lead to stabilization of metastable phases and improved phase purity. According to Boltersdorf et al, flux-mediated single crystal growth can be described in four steps: i) reactant dissolution; ii) reactant diffusion through the molten flux; iii) nucleation, and iv) subsequent crystal growth of the product from the nuclei [25]. While in traditional solid state synthesis, high temperatures and relatively long time are necessary to allow ion diffusion, the rate of which is often a limiting factor, the improved kinetics of salt-melt fluxes help to overcome such boundaries by improving homogeneity in the reaction. In designing a synthesis, Liu et al. [26] recommend using the hard-soft acid-base (HSAB) theory as a simple guide to determine which reactants to use: hard, non-polarizable prefers hard and soft, polarizable prefers soft. Hydroxides are small, electron-dense hard bases. The metal hydroxide we choose must then be hard, or a “borderline” hard, metal to favor dissolution, such as Nickel(II) or Copper(II). A more in-depth theory to describe the melt uses the Lux-Flood concept of oxo-acidity where H_2O and O^{2-} serve as the acid and the base, respectively [27, 28]. The Lux-Flood concept requires the use of a new dissociation constant,

$$K_d = \frac{[H_2O][O_2]}{OH^-} \quad (1)$$

K_d is an indicator of the basicity of different alkali bases, and is affected by the charge density of the metal cation and temperature. Prior to Zhou’s work, hydroxide fluxes alone had not been used as a reaction medium for chalcogenides [29]. They found that phase selection can be further controlled by two key parameters: the sulfur concentration and solubility of the melt.

The initial goal of this project was to replicate the synthesis of KNi_4S_2 and optimize the molten hydroxide flux method to produce larger single crystals so that we could better explore their magnetic and physical properties. Through tuning the synthesis parameters, I have been able to grow single crystals larger than those previously re-

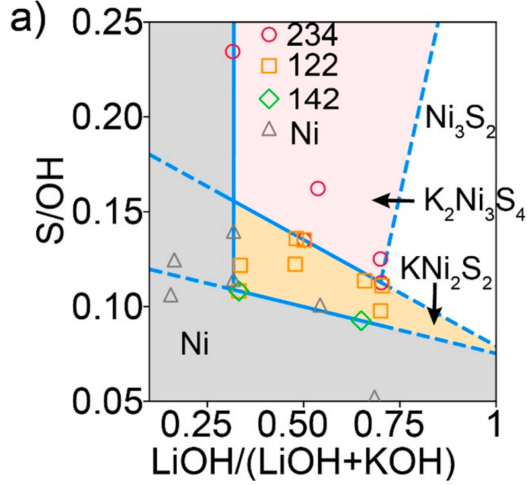


FIG. 1. (a) Phase diagram of sulfur concentration vs. concentration of lithium hydroxide. Measured by Zhou et al. [21].

ported, as seen in Fig. 4. Our synthesis has led to the first reported magnetization, resistivity and heat capacity measurements of this newly discovered system for both polycrystalline and single crystal samples. In addition, we learned to synthesize other nickel sulfide systems, KNi_2S_2 and $\text{K}_2\text{Ni}_3\text{S}_4$, by simply tuning the temperature profile while keeping the stoichiometric ratios constant. The XRD and magnetization data for these additional phases are also reported.

III. EXPERIMENTAL METHODS

A. Single Crystal Synthesis

The flux growth of KNi_4S_2 single crystals starts by thoroughly mixing nickel (II) hydroxide, and oven-dried elemental sulfur (5N) in a 1:2.5 molar ratio along with reagent grade lithium hydroxide (2N) and semiconductor-grade potassium hydroxide in a 0.3:0.7 molar ratio. All hydroxides were purchased from Sigma Aldrich. The mixture is then loaded into a vitreous carbon crucible in order of decreasing melting points: the nickel (II) hydroxide/sulfur mixture is placed below the lithium hydroxide/potassium hydroxide mixture. Vitreous carbon is necessary in this synthesis because the traditional alumina crucible reacts with KOH. The strong interaction between potassium ions and alumina oxide was observed by Walspurger et al. in their experiments [31]. The reaction vessel is placed in a programmable Lindberg tube furnace under a constant flow of argon

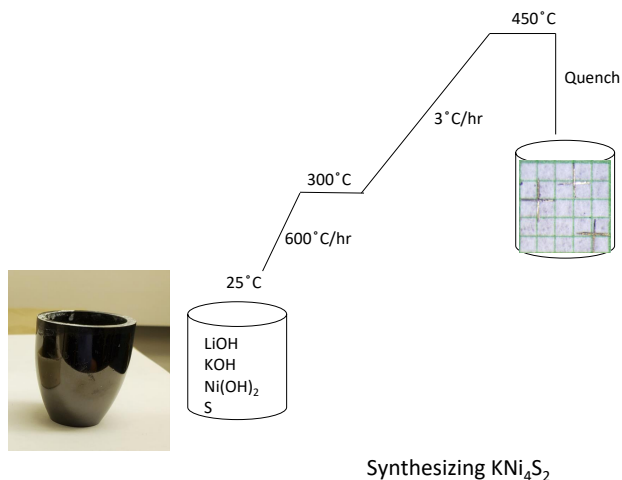


FIG. 2. The temperature profile for 142 phase. The reactants are placed in an open vitreous carbon crucible and are rapidly heated in an argon-filled tube furnace to 300°C , which is above the eutectic temperature (Fig. 3) of our chosen flux [30]. Then, the reaction is slowly warmed to a maximum temperature, to encourage the nucleation of our desired phase. Finally, the reaction is rapidly quenched to preserve the kinetically stable phase before decomposition. This synthesis method is unique because the crystals form while the temperature is slowly increased rather than during the slow cooling used in traditional flux growth synthesis.

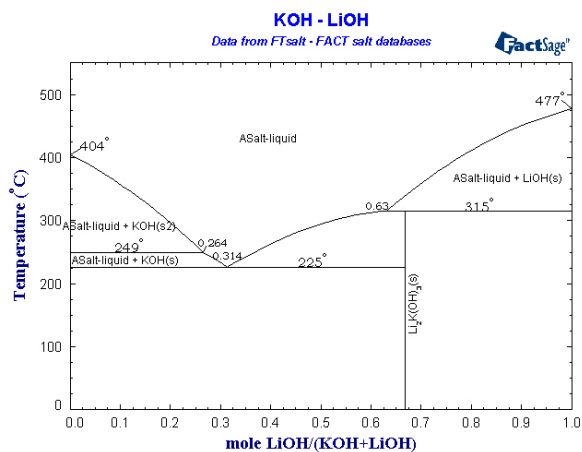


FIG. 3. KOH-LiOH Phase Diagram

(45 cc/min). The reaction is heated to 300°C in half an hour and then slowly warmed up to 450°C at $3^\circ\text{C}/\text{hour}$. Once the maximum temperature is reached, the heating elements are turned off and reaction is furnace-cooled (which we also refer to as quenching). This synthesis is adapted from Dr. Xiuquan Zhou [21]. The crystals are separated from the solid flux by sonication in Deionized (DI) water for 20 minute intervals, followed by washing in ethanol after filtration. The resulting crystals are shown in Fig. 4.

I found that the ramp rate was an additional parameter that played a critical role.

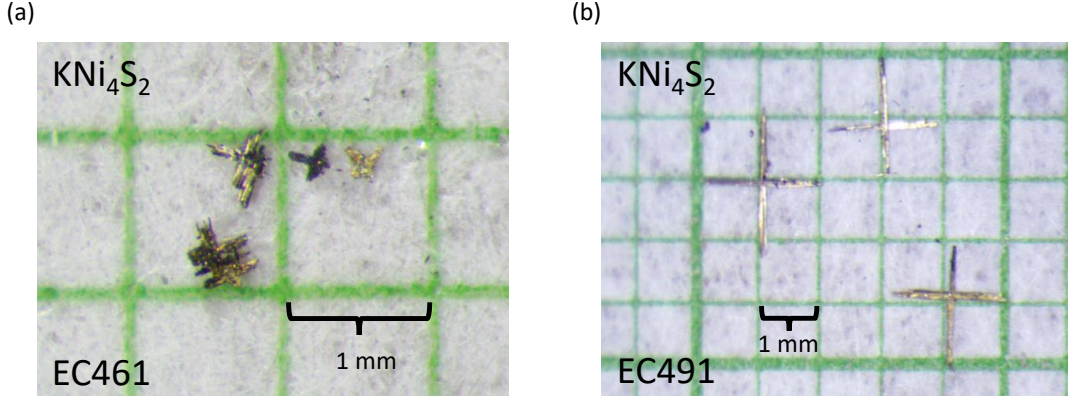


FIG. 4. (a) My first successful batch of KNi_4S_2 crystals were consistently the sub-millimeter size reported in previous literature [21]. (b) After several trials of tuning the synthesis parameters, I was able to grow samples of the 142 phase up to 2 mm long. This dramatic improvement in the size of the crystals enabled us to study the anisotropic magnetic properties.

When following the temperature profile in Fig. 2, the 142 phase is consistently produced. However, I found that by changing the temperature profile without changing the stoichiometry of the reactants, the KNi_2S_2 and $\text{K}_2\text{Ni}_3\text{S}_4$ phases, could easily be produced in much larger crystals than previously reported. To explore these phases, the cool down rates were shortened until eventually revealed to be unnecessary. In addition, the dwell times at the maximum temperature were lengthened and shortened and the initial ramp rate was changed in a variety of increments, the details of which can be found in Table I and Table II. Eventually, the temperature profile to produce each phase was discovered. To synthesize KNi_2S_2 , the ramp rate was increased to $900^\circ\text{C}/\text{hr}$ to a maximum temperature of 450°C , and allowed to dwell for 30 hours before being quenched. With this temperature profile, depicted in Fig. 5, KNi_2S_2 crystals with 2 – 3 mm dimensions were produced.

In addition, while trying to optimize the 142 synthesis, I found that if too long of a dwell time or ramp rate was used, $\text{K}_2\text{Ni}_3\text{S}_4$ was produced in crystals up to 2 mm in size. A temperature profile that will produce the 234 phase is shown in Fig. 6. Although the 122 and 234 phases were not the desired phases, knowing how and when they form can give us a glimpse into the kinetics, thermodynamics and stability of each of the three phases. I believe that the oxidation state of each phase plays a role in their relative stability. The 142 phase is the kinetically favored product and contains a +0.75 oxidation state on the nickel site (assuming ionic bonding). When the mixture is

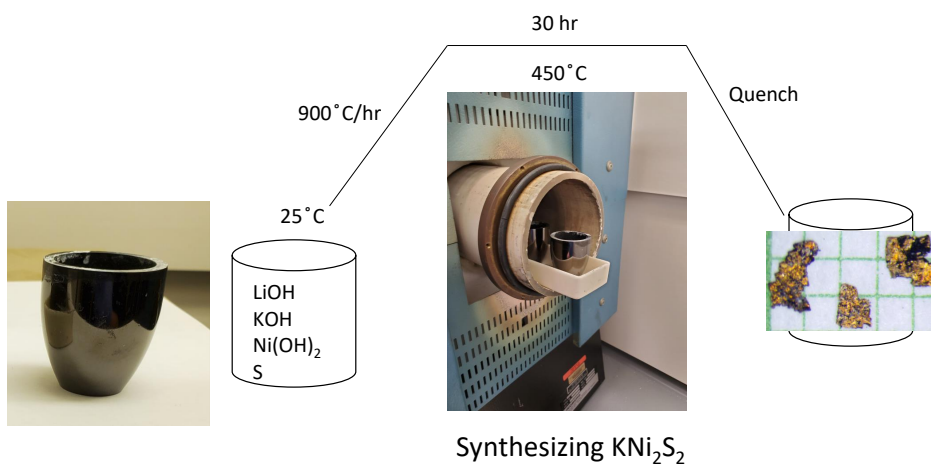


FIG. 5. Temperature profile for 122 phase. The reactants are placed in an open vitreous carbon crucible and are rapidly heated to 450°C in an argon-filled tube furnace. The reaction is held at this maximum temperature for 30 hours before it is quenched to yield KNi₂S₂ crystals.

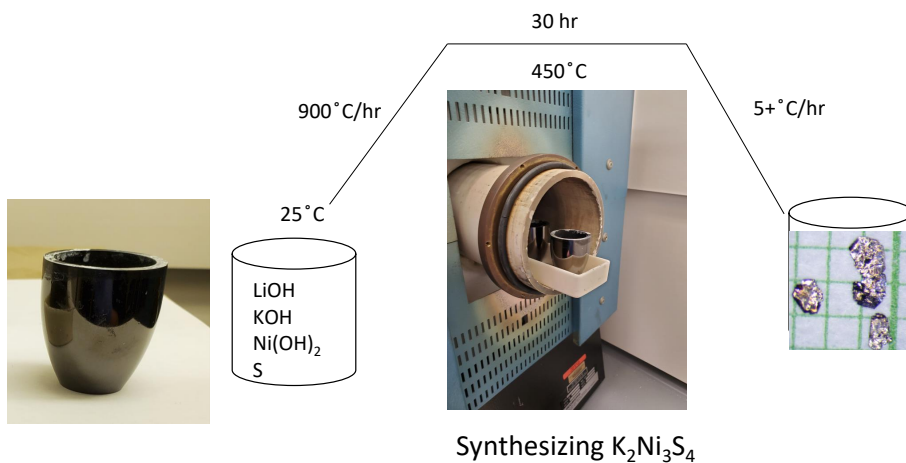


FIG. 6. Temperature profile for the 234 phase. The reactants are placed in an open vitreous carbon crucible and are rapidly heated to 450°C in an argon-filled tube furnace. The reaction is held at this maximum temperature for 30 hours before it is slowly-cooled to yield K₂Ni₃S₄ crystals.

allowed to dwell at 450°C, we see that the 122 phase, which has a more favorable +1.5 oxidation state on the nickel sites, is dominant. Finally, when allowed to dwell and cool for even longer, the 234 phase is the prevailing phase since it has a +2 oxidation state which is nickel's desired and most stable oxidation state. Therefore, we conclude that K₂Ni₃S₄ is the thermodynamically stable phase, while the others are only metastable.

B. Powder X-Ray Diffraction

After the crystals are synthesized according to the methods described in the previous section, we use X-ray diffraction to characterize the crystal structure of our samples to ensure we grew the correct phase. X-ray diffraction is a common technique which has been around since the early 1900s, grounded in the principles of Bragg’s law: $n\lambda = 2d\sin(\theta)$. X-rays with a wavelength (λ) diffract off of the periodic spacing between atoms separated by a distance (d) at an incident angle (θ) that is picked up by the detector producing a unique diffraction pattern for each compound. These patterns can tell us the symmetry associated with the compound’s crystal structure and atomic placement.

We use a Rigaku MiniFlex 600 Powder X-Ray Diffractometer (PXRD) and analyze the resulting diffraction pattern with Rigaku PDXL 2 analysis software to compare the collected spectra to the available Crystallographic Information File (CIF). Since the CIF for the 142, 122, and 234 phases were previously reported [21], we were able to identify each phase we grew. While we typically grind our single crystal samples into a powder to get diffraction peaks from all crystallographic orientations, I found these samples were difficult to grind into a powder with a mortar and pestle. Furthermore, grinding broadened any peaks in the XRD pattern making them illegible. Since the crystal axes’ relationship to how the crystal grows physically was previously unreported, XRD was performed on single crystals which were rotated after each measurement to identify the a , b , and c axes. For example, we learned that the 142 phase prefers to grow in thin needles along the c axis while the a and b axes tend to have similar dimensions. By identifying the different axes of our single crystals, we can study the directional dependence, or anisotropy, of the compounds’ magnetic and physical properties.

C. Magnetic Characterization

We use a Magnetic Property Measurement System (MPMS) XL developed by Quantum Design to measure magnetization as a function of temperature ($2\text{ K} < T < 300\text{ K}$) and applied field ($-7\text{ T} < H < 7\text{ T}$). The MPMS uses a Radio-Frequency Superconducting Quantum Interference Device (RF SQUID, or simply SQUID) to measure a change in magnetic flux through a pickup loop [32]. By measuring the change in flux

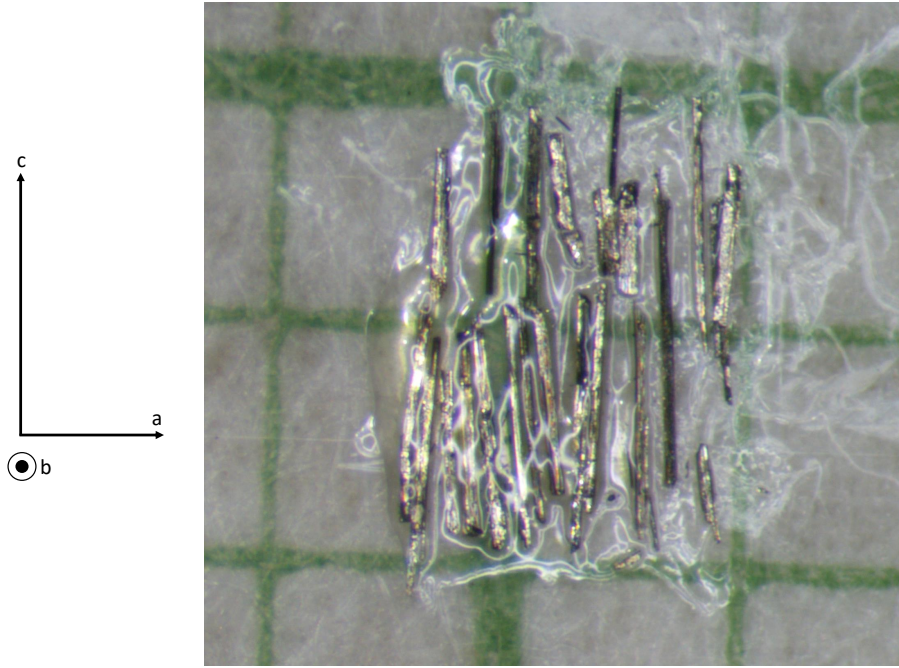


FIG. 7. A mosaic of KNi_4S_2 single crystals aligned for magnetization measurements.

as a sample is moved through the pickup loop, the MPMS can measure the magnetic moment of the sample.

Despite the incredible sensitivity of the SQUID, we found it difficult to get a good signal when measuring the KNi_4S_2 samples. This difficulty is due to the measured magnetization being proportional to the magnetic moment of the sample, and the mass of the sample itself. In the case of the 142 phase, the single crystals are both small (sub-milligram) *and* contain a small magnetic moment. As a result, multiple attempts at measuring a single crystal with a variety of mounting methods were performed, but the signal proved to be too small. For example, with delicate samples such as KNi_4S_2 , we usually use a small amount of Apiezon N vacuum grease to affix the sample to a long, rectangular strip of plastic transparency slide fit into a straw. While this method keeps the sample intact and well-centered in the SQUID pickup loops, in this case, the diamagnetic contribution of the grease overcame the sample's magnetic signal. This method was used for my pellet sample since the increase in mass dwarfed the diamagnetic contribution from the grease.

I found that the solution to the small sample signal was to simply use more sample. First, I loaded many crushed single crystal samples totalling a mass of 24 mg into a gel cap. Although this is a “polycrystalline” measurement and we lose any information

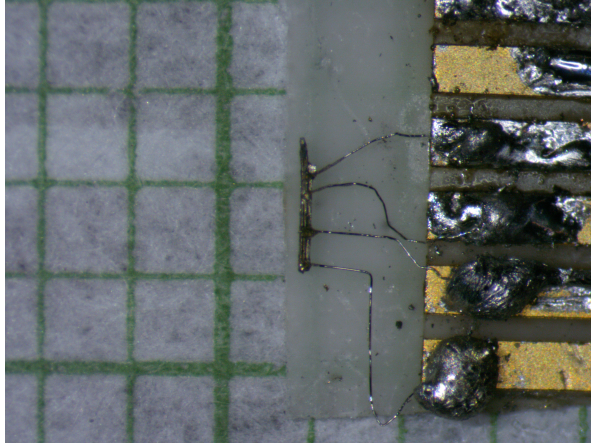


FIG. 8. A KNi_4S_2 single crystal sample wired with 0.001 in diameter platinum wires affixed with silver epoxy for resistivity measurements in a PPMS. This photograph was taken on mm-grid paper.

about the anisotropy of the sample, it was a good first step to characterizing its magnetic properties. In order to measure the 142 phase's directional dependence, I made a mosaic of 24 single crystals held in place on a piece of transparency with a small amount of Apiezon N grease, as shown in Fig. 7. The mosaic had a mass totalling 0.17 mg and it was possible to align the crystals because the a , b , and c axes are clearly identifiable.

D. Resistivity

Resistivity measurements were done using the four probe method on both a single crystal (data shown in Fig. 17) and a pressed polycrystalline pellet. By using the outer two probes to provide a constant current and the inner two probes to measure a change in voltage, we can isolate the sample resistance, R , and avoid measuring any contact or wire resistance. Knowing both the voltage drop and the current applied, we use Ohm's law, $V = IR$, to find the resistance of the particular sample.

To measure the resistance, R , we use a Quantum Design Physical Property Measurement System (PPMS). The PPMS can measure the sample's resistance as a function of temperature from 300 K to 1.8 K at various fixed fields, including zero field, or resistance as a function of applied field from -14 T to 14 T at a given temperature. In the resistivity equation, A is the cross sectional area and L is the distance between the voltage leads. Then, using $\rho = R(A/L)$ the resistivity ρ , which is an intrinsic property of the material, can be calculated. To calculate the area and distance between leads on such a

small sample, the sample is photographed against millimeter grid paper and the photo is analyzed using an online photo measuring tool (<https://eleif.net/photomeasure>) to measure the resulting lengths, the margin for error in this portion is quite large so a maximum distance of L is desired to give a more accurate value. To set up this measurement, 0.001 inch diameter platinum wires are affixed to the sample with a two-part silver epoxy, EPO-TEK H20E in this case. Once the epoxy is cured in an oven, the leads are soldered to a “platform” that has gold conductive strips on an insulating substrate. This platform, shown in Fig. 8, is necessary to mechanically stabilize small and thin samples that are prone to breaking. The platform is then mounted to an AC transport sample puck. Once the sample is mounted to the puck, a small DC current ($\approx 1 - 10$ mA) is applied through each combination of leads to anneal any defects in the wire or epoxy connection. The annealing process is performed until a desired resistance is achieved, less than 10Ω for a metallic sample such as this one. Measuring resistivity allows us to check the Residual Resistivity Ratio (RRR) to learn about the quality of the sample, and how the electrons in the system behave when a transition occurs.

E. Heat Capacity

Heat capacity is yet another measurement in our experimental arsenal that gives us a glimpse into what is happening in the material with regards to the behavior of the lattice, electronic and magnetic properties. In order to set up this measurement, an addenda must first be taken which measures the heat capacity of the Apiezon N vacuum grease in $T < 200$ K or Apiezon H grease if $T > 200$ K and the measurement puck alone to account for the background heat capacity. Next, the sample is placed in the mounting grease ensuring good thermal contact between the sample and the platform, and the exact same measurement is redone. The heat capacity puck uses its heaters on the platform coupled with a thermometer to warm the sample a certain amount and the sample is allowed to slowly cool back down which is called a relaxation technique, which allows us to measure the thermal changes in the system. For a ferromagnetic system, a phase change should be seen in heat capacity. Measuring heat capacity in superconductors, however, is uniquely useful as not only will the superconducting transition be observed, but the amount of superconducting response in your sample can be quantified by subtracting out the any heat capacity contributions from non-superconducting defects in

the material. Since the physical properties of many of these nickelate compounds are yet to be reported, they may be ferromagnetic, or superconducting, or both, and heat capacity could give us new insights into the materials.

IV. RESULTS AND DISCUSSION

A. KNi_4S_2

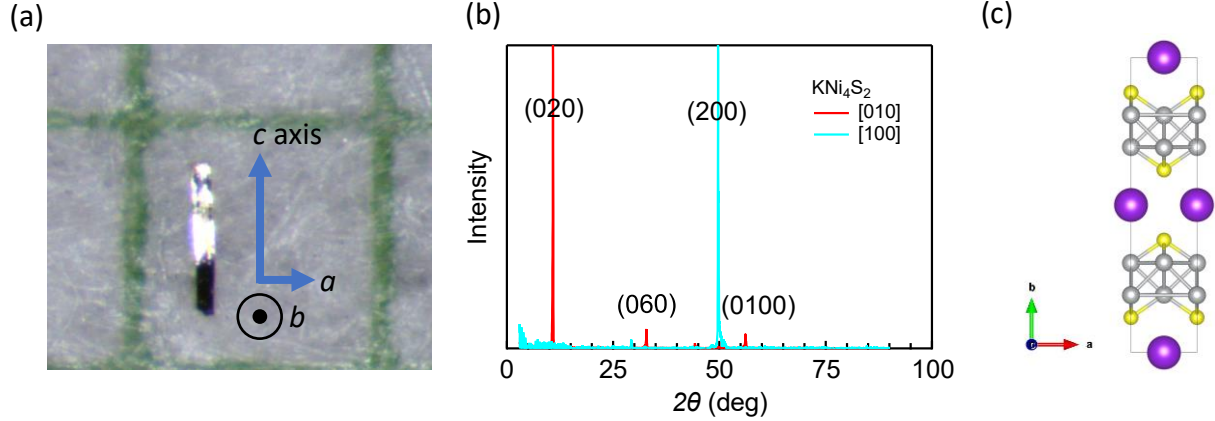


FIG. 9. (a) A 142 phase single crystal on mm grid paper with the axes labelled. (b) Single crystal XRD pattern along the a and b axes. (c) KNi_4S_2 crystallizes in the $Cmmm$ space group.

1. Synthesis

We observed that during the reaction, phase selection relied primarily on the basicity of the melt and the temperature profile used. Since KOH and LiOH are hygroscopic, too slow of a warming rate produced a more acidic melt than was favorable for the 142 phase. My synthesis notes are compiled in Tables I and II. Every furnace is different so there will be some degree of adaptation required. The first dozen batches resulted in little to no yield of the desired phase in single crystal form. We finally saw success after increasing the ramp rate from 3°C to $15^\circ\text{C}/\text{min}$. It is important to use a higher ramp rate to minimize the dwell time at lower temperatures where the melt is KOH rich due to the lower melting point of KOH compared to LiOH. Once single crystal samples were synthesized, XRD analysis allowed us to determine axial orientation which was previously unreported and important for the following anisotropic magnetization measurements. Another challenge necessary to overcome was the consistent twinning seen in the 142 phase for magnetic measurements. As seen in Fig. 4b, the samples like to form in crosses, which make measuring anisotropy difficult. After tailoring the

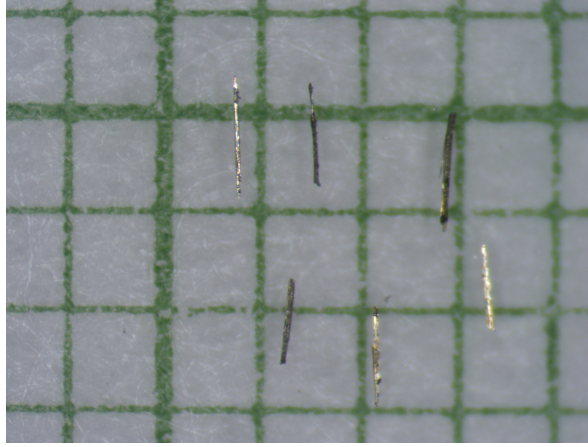


FIG. 10. Samples of KNi_4S_2 crystals without twinning. The samples are slightly smaller than the twinned samples, however, the magnetic anisotropy can be truly measured since there is no longer an additional contribution from a different axis. The size difference did pose a challenge in mounting for resistivity measurements but the long bar shape is ideal for measuring with $I \parallel c$ and this difficulty was overcome.

temperature profile and quenching at different points in the reaction, we found that untwinned samples can be produced with a sacrifice to their relative size, as shown in Fig. 10. A longer warm up time is needed, so a fast ramp rate ($900^\circ\text{C}/\text{hr}$) was used until 225°C before the reaction was slowly warmed over 45 hours to 450°C , allowed to dwell for 15 hours and then furnace-cooled. Afterwards, the crystals are cleaned in the same manner discussed in the previous experimental methods.

2. Magnetization Data

Polycrystalline samples were prepared using two different methods. A gel cap method, in which samples were placed in a gelatin-based capsule, the capsule is packed with cotton to secure the samples in place, the capsule is then punctured to allow evacuation of oxygen and the entire capsule is placed in a plastic beverage straw and lowered into the MPMS sample chamber. The second method involved loading an amount of sample into a quarter-inch diameter die made by MP corporation and using a hydraulic press with upwards of 2 metric tons of force to compress the crystals into a pellet. This pellet is then adhered to a Mylar strip using Apiezon M grease and again placed into a plastic beverage straw and lowered into the machine. Both data sets revealed similar transitions, however, the magnetization values for single crystals were better represented in the pressed sample. Both data sets, polycrystalline and pellet,

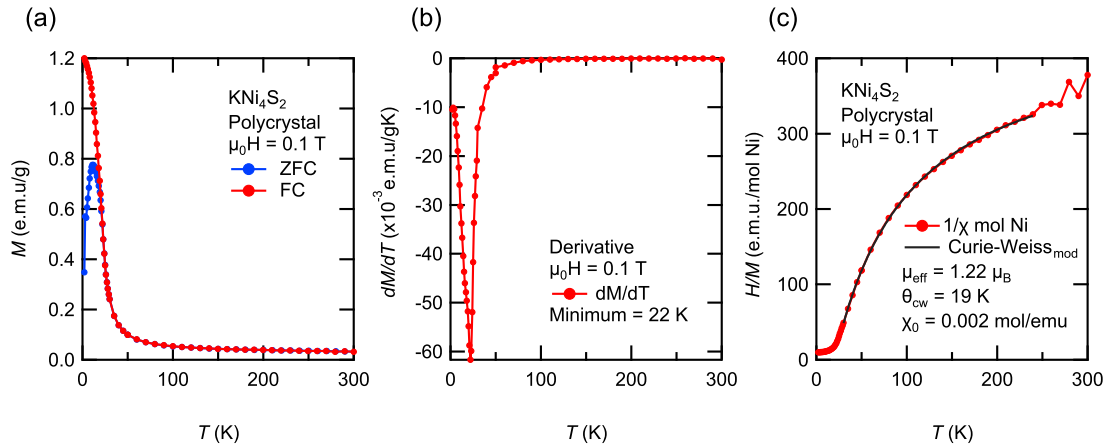


FIG. 11. (a) Field-cooled (FC) and Zero-field-cooled (ZFC) magnetization versus temperature for polycrystalline sample at 0.1 T. (b) The temperature derivative of the FC magnetization shows a distinct minimum which suggests a $T_C \approx 25$ K. (c) By plotting H/M v. T , we can fit the high temperature region to a modified Curie-Weiss law to extract the effective moment (μ_{eff}) and Curie-Weiss temperature (θ_{CW}). We find that $\mu_{\text{eff}} = 1.22 \mu_B/\text{Ni}$, which is consistent with Ni being in a lower oxidation state than Ni^{1+} for which we would expect $\mu_{\text{eff}} = 1.7 \mu_B$.

are included in this thesis, the results of which are shown in Fig. 11 and Fig. 14, respectively. I measured M for single crystal samples along the three different axes, using a variety of mounting methods due to the size of the untwinned samples and their weak magnetization. When a single crystal was used, the diamagnetic contribution of our mounting grease (Apiezon N vacuum grease) dominated the sample's magnetic signal. To overcome this, a mosaic was created and rotated to the appropriate axes. Magnetization data suggests the samples are relatively isotropic in nature along the a and c axes, however the magnetization along the b axis is visibly higher. These results make sense considering the relative lengths of the crystal structure.

Interestingly, the 142 phase demonstrates distinct features associated with ferromagnetism. When examining the magnetization versus temperature (M v. T) curves in both zero-field-cooled (ZFC) and field-cooled (FC) methods at 0.1 T for polycrystalline and 0.5 T for single crystal, there is a distinct difference in values. This difference is a signature of the formation of ferromagnetic domains, along with domain wall pinning. When the first derivative of this M v. T curve is taken, we find a minimum around $T = 25$ K for both polycrystalline and single crystal data, which gives us an idea of the Curie temperature. The crystal structure is orthorhombic with $a = 3.6617 \text{ \AA}$, $c = 3.6694 \text{ \AA}$, and $b = 16.3810 \text{ \AA}$.

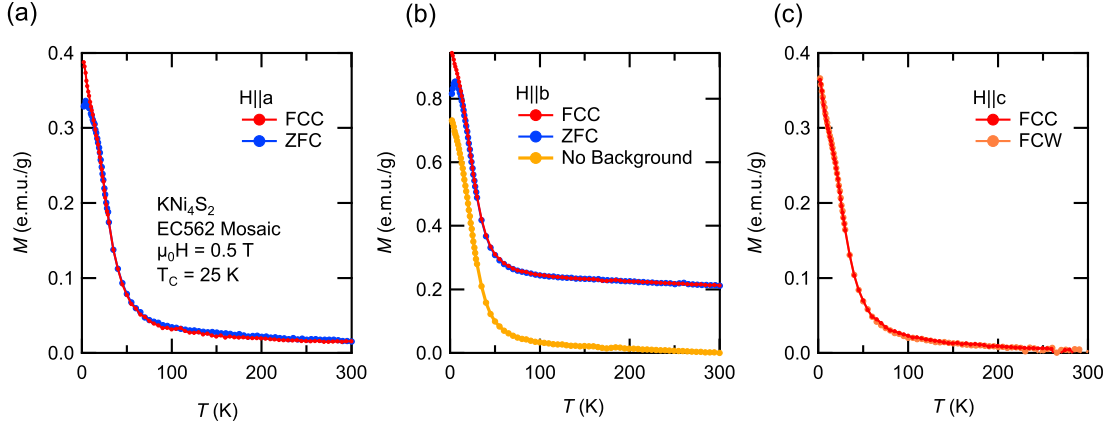


FIG. 12. We measure the field-cooled-cooling (FCC) and zero-field-cooled (ZFC) magnetization as a function of temperature along the (a) a axis, and (b) b axis in a 0.5 T applied field. (b) FC and ZFC magnetization curves along the b axis at $H = 0.5$ T with and without subtracting a temperature independent background. (c) FC and field-cooled-warming (FCW) magnetization curves along the c axis with $H = 0.5$ T.

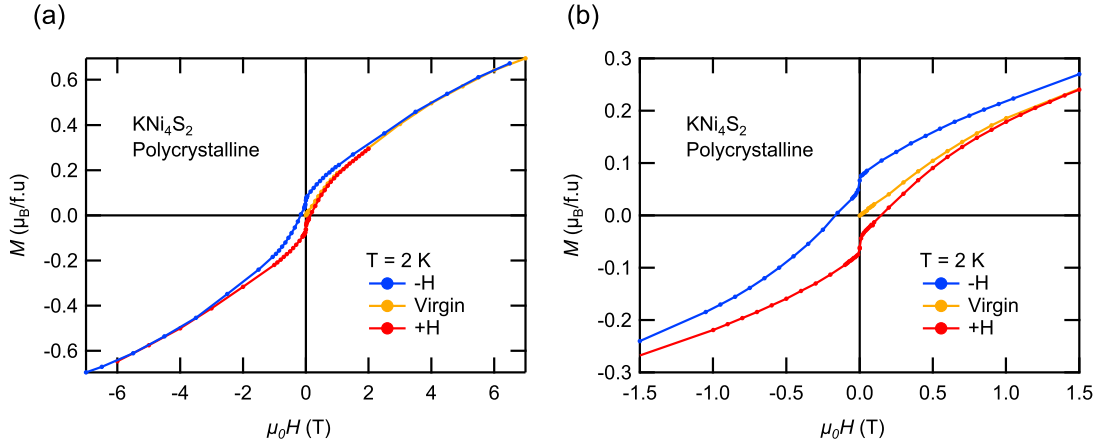


FIG. 13. (a) Full M v. H on a polycrystalline sample at $T = 2$ K (b) By zooming in, we can clearly see the hysteresis loop, the remanent field, and the coercive field. These are features that suggest a ferromagnetic phase.

When analyzing the magnetization versus field (M v. H) we see additional signs of ferromagnetism: in the polycrystalline sample the presence of a hysteresis loop with a coercivity of 0.15 T (at $T = 2$ K) and a remanent magnetization at zero field is apparent.

The value of M at 7 T for the polycrystalline sample is over a factor of two larger than that collected from the single crystal mosaic. To investigate this discrepancy, I remeasured M v. H on a pellet. The pellet pressing method involves loading 1.14 mg of hand-selected clean single crystals into a die and using a hydraulic press with upwards

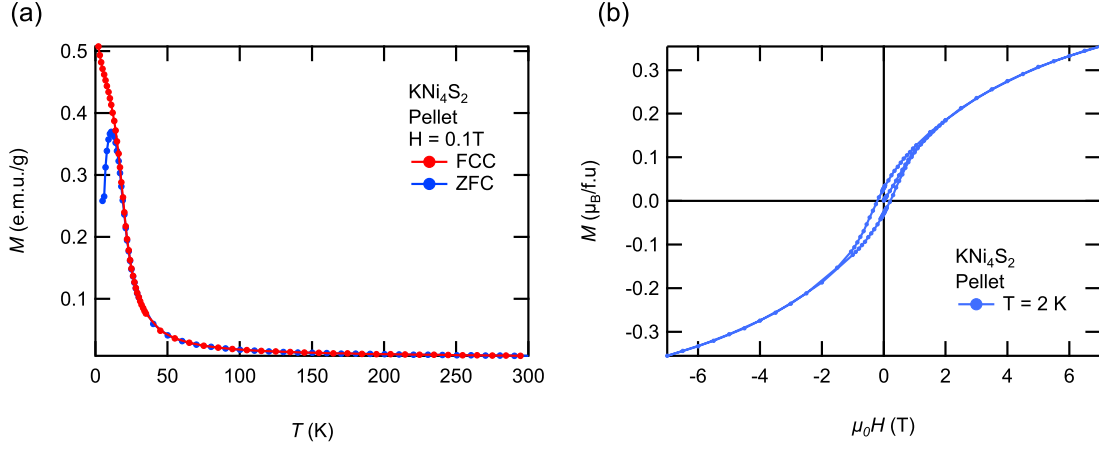


FIG. 14. In this figure, clean single crystals were selected and pressed into a pellet. (a) MvT and (b) MvH .

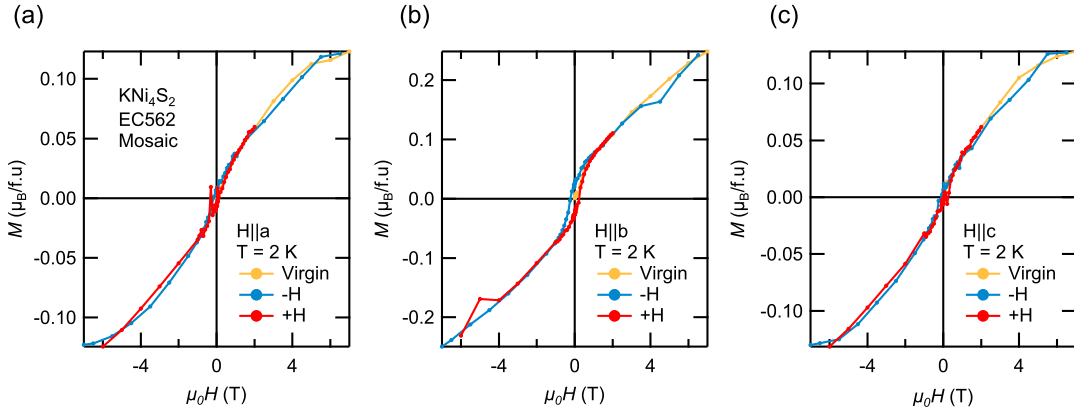


FIG. 15. $M v. H$ along the (a) a axis, (b) b axis and (c) c axis. These anisotropic measurements suggest that the b axis is the easy magnetic direction since M along the b axis twice as large as M along the a or c axes, and since the b axis exhibits hysteresis whereas the other axes do not.

of 2 metric tons of force to compress the sample together. From the pellet data, $M v. H$ shows roughly the same magnitude as the mosaic when measured along the b axis, which is no surprise. In addition, $M v. T$ from the pellet is more consistent with the mosaic data. This experiment shows that if more sample mass is necessary to get a good magnetic signal, making a pellet of clean signal crystals will yield more accurate results compared to a polycrystalline sample which may have small impurities of other phases.

Single crystal axial measurements show the magnetization appears to be relatively isotropic along the a and c axes. Along the b axis, however, we see the appearance of a

small hysteresis loop as seen in the polycrystalline data. These are additional distinct calling cards of ferromagnetic domains. An applied magnetic field of 7 Tesla was not enough to achieve magnetic saturation for either the polycrystalline or single crystal samples which further corroborates our inclination that the sample is a weak itinerant ferromagnet. The b axis also has a much larger magnetization value which alludes to this being an easier axis than a or c .

In examining the magnetic properties we need to distinguish between local moment and itinerant ferromagnetism. Since the ternary compound contains nickel, we would expect to see local moment ferromagnetism on the nickel site to an order of $1 \mu_B$ per atom. However, we see a much smaller moment in our measurements on both polycrystalline and single crystal samples. This observation leads us to agree with Zhou's conclusion that the sample is a weak itinerant ferromagnet, although their data has not been published for comparison [21].

The obscure background seen along b was temperature-independent, and appeared to be proportional to our applied field. When measurements were taken at 0.1 T and 1 T, the background shifted accordingly. When the background is subtracted out, the data still fits our hypothesis that b is our easy magnetization axis when compared with a and c . The presence of the background is puzzling since the reported goodness of fit along b is significantly better than that along a or c (see Fig. 26).

To ensure the ferromagnetic features seen in the material are not due to some magnetic impurity (e.g. a small amount of un-reacted Ni), M v. H is measured at $T = 300$ K. The idea is that the presence of Ni impurities would be visible (such as in hysteresis or a remanent field) at 300 K, since the T_C of Ni is 627 K. When we fit a line to the curve, we find the remanent magnetization at $\mu_0 H = 0$ T is $0.00018 \mu_B/\text{f.u.}$ In conclusion, this magnetization is negligible, and we do not believe it is responsible for the magnetization we observe at low temperatures.

3. Resistivity

The results of the resistivity measurements on a KNi_4S_2 single crystal are shown in Fig. 17. The Residual Resistivity Ratio (RRR) is defined as $\rho(300 \text{ K})/\rho(2 \text{ K})$ and gives an idea of the sample quality. For this particular sample, I measure a RRR of 44 which usually indicates good sample quality.

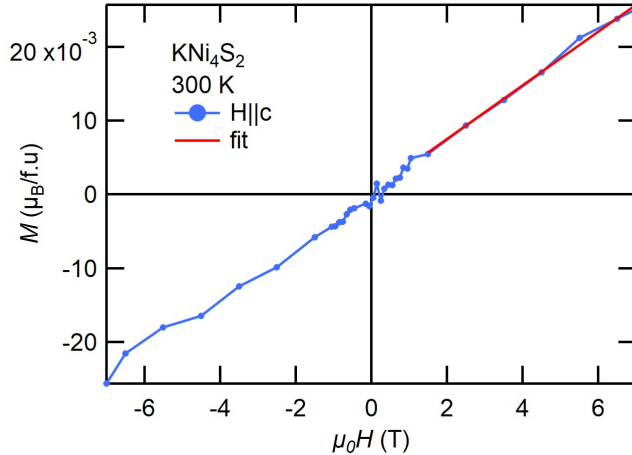


FIG. 16. M v. H along the c axis at room temperature. We fit a line to the high field points and find the y -intercept to be $M = 0.00018 \mu_B$ which is negligible.

Since T_C is defined as the spontaneous alignment of magnetic moments in zero field, resistivity measurements, which can be performed at zero applied field (unlike magnetization measurements in the MPMS), could potentially confirm the $T_C \approx 25$ K suggested by our magnetization data. Usually, the ferromagnetic ordering of local moments causes a drop in ρ which would appear as a discontinuous increase in the derivative, $d\rho/dT$. Although we consistently measure a minimum in dM/dT at 25 K, we do not find a corresponding feature in ρ or $d\rho/dT$. It has been shown, however, that a feature in resistivity might not appear in weak itinerant ferromagnets without some additional smooth background subtraction, in the case of Yelland et al, that background was $\rho + AT^2$ to fit the data better [33]. I also measured resistivity as a function of applied field in Fig. 17c to check for any field-induced transitions or other anomalies. None were found.

4. Heat Capacity

My heat capacity measurement on a KNi_4S_2 polycrystalline pressed pellet (1.82 mg) is presented in Fig. 18. This is the first-reported heat capacity measurements. Although we do not observe a phase transition at $T = 25$ K as suggested by our magnetization data, given how small the magnetic moment is suspected to be, this is not unusual. For example in ZrZn_2 , a weak itinerant ferromagnet, a feature of the FM transition is extremely small and only seen when the isolating the magnetic contribution to the

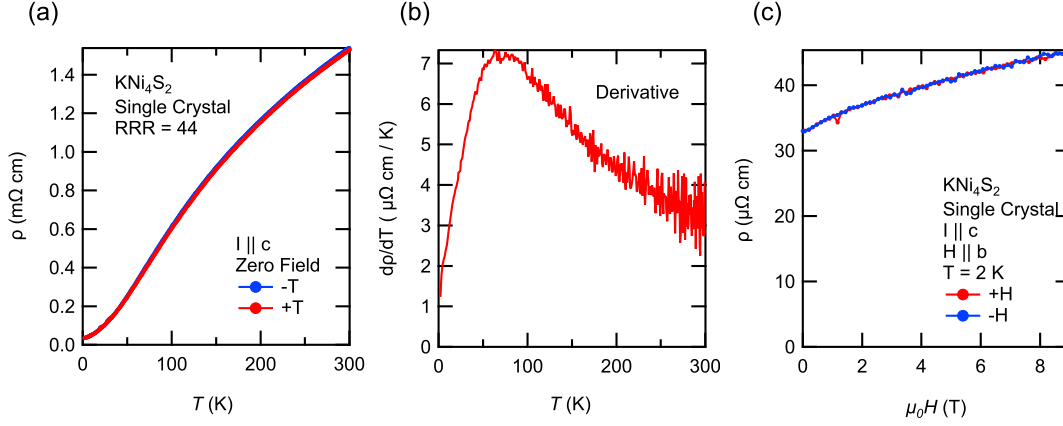


FIG. 17. (a) Resistivity in 142 phase with current along the c axis. The Residual Resistivity Ratio (RRR) = 44 which is reasonably high showing good quality. (b) The derivative of ρ v. T in search of a feature associated with our transition temperature. (c) ρ v. H to check for field-induced transitions and to study the magnetoresistance of the material.

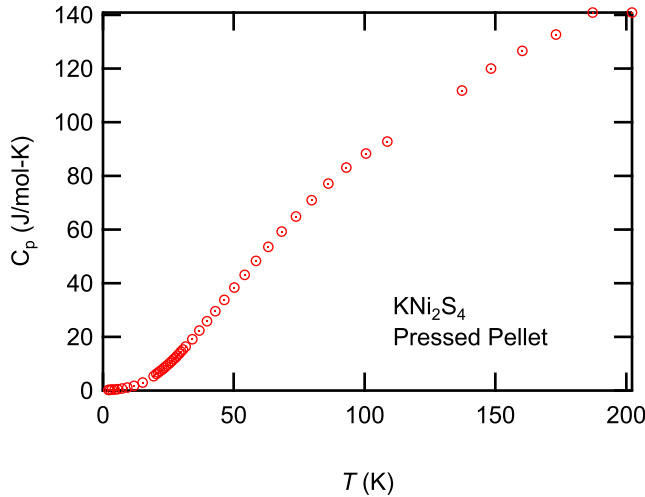


FIG. 18. The first-reported results of heat capacity on a 142 polycrystalline pressed pellet sample. We do not observe a phase transition at $T = 25$ K.

heat capacity by subtracting out a background consisting of electronic and phonon contributions [33]. In addition, it is even possible to have a small signal at T_C in heat capacity in systems with large magnetic moments. For example, LaCrSb_3 is a ferromagnet with a $1.6\mu_B$ magnetic moment, but the transition in heat capacity is similarly only observed when the signal from its nonmagnetic counterpart (LaVSb_3) is subtracted [34, 35]. Larger single crystal samples may be needed, as well as a good model for the heat capacity background before we observe features in the heat capacity of this 142 phase.

B. KNi_2S_2

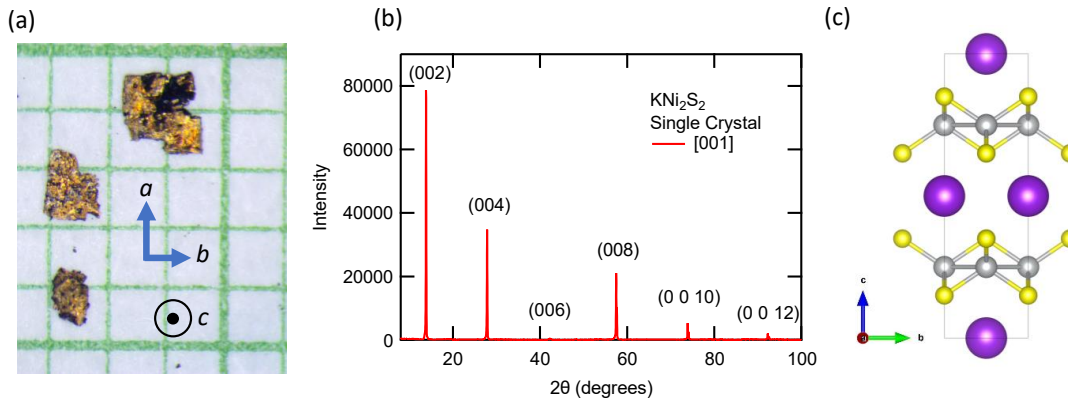


FIG. 19. (a) Samples of KNi_2S_2 photographed on mm-grid paper with the crystal axes labelled. The samples have a distinct gold color. (b) With a clean, freshly-made sample, the XRD pattern for a 122 single crystal shows sharp peaks associated with the c axis, as expected for measuring a single crystal in this orientation. (c) The 122 phase is tetragonal and crystallizes in the $I4/mmm$ space group

1. Introduction

With the 142 phase being isostructural to some cuprates, we see that the 122 phase shares its structure type with another very common superconductor type, the 122 family of iron-based superconductors. KNi_2S_2 crystallizes in the ThCr_2Si_2 structure type, with a $I4/mmm$ space group. Although the iron based superconductors are not known for having as high critical temperatures as the cuprates, they can still possess superconducting transitions up to 56 K for the iron arsenides [36]. Other interesting features are still studied in this group with materials such as KFe_2As_2 which has a superconducting transition at around 3.5 K and changes its superconducting gap structure under pressure [37]. Because this 122 family is still an active area of research on unconventional superconductivity, KNi_2S_2 crystals have the potential to be the next link in monitoring how changes in pressure and chemical substitution can affect superconducting transitions. While KNi_2S_2 was found to be superconducting at $T_c = 0.46$ K [38], prior to the work by Zhou et al. [21], only polycrystalline samples of KNi_2S_2 were synthesized. Zhou et al. were able to synthesize the first-known single crystals from this hydroxide flux

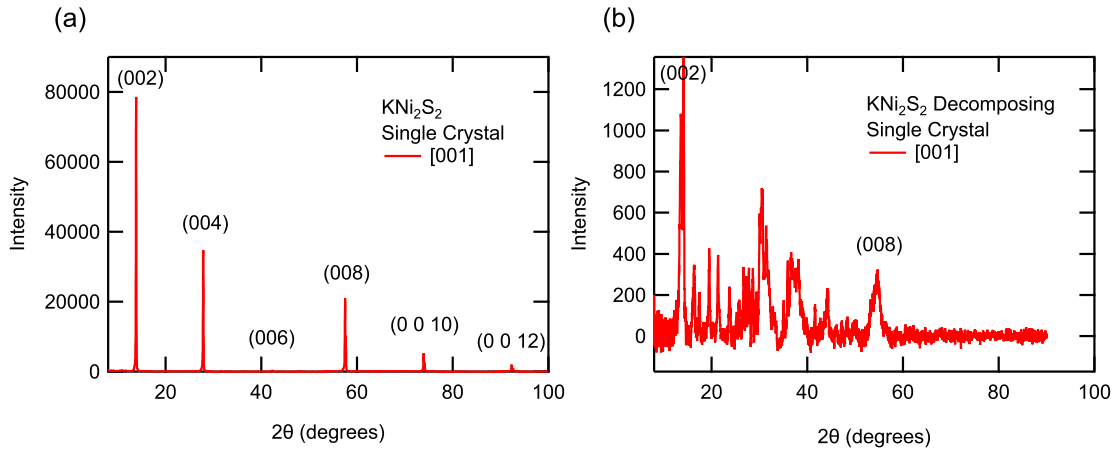


FIG. 20. (a) With a clean, freshly-made sample, the XRD pattern for a KNi_2S_2 single crystal shows sharp peaks associated with the c axis as expected for measuring in this orientation. (b) After being exposed to air for some time, the 122 phase decomposes and the XRD pattern shows significant degradation. The (002) and (008) peak intensities are dramatically reduced and many new small peaks appear. More research is necessary to determine how exactly the 122 phase decays.

method, though their limitation was size, only achieving samples on the order of 200–300 μm . By improving on their original recipe, I was able to synthesize single crystals 2 – 3 mm long with a variety of widths, as shown in Fig.19a. The larger samples will allow for physical property measurements and sample quality determination in future work. A major caveat to the 122 phase, is its metastable nature and its tendency to decompose. Our work concludes with the XRD pattern and magnetic properties of the material.

2. XRD

The x-ray pattern for a “fresh” 122 single crystal is shown in Fig. 20a. Although it was only a 4 hour scan, I obtained strong diffraction peaks for the c axis that match the previously reported angles. Leaving KNi_2S_2 on the lab bench makes it turn grey and handling it will turn it into a powder. Whether the sample oxidizes or decomposes is still to be determined, although placing it in a vacuum oven at 100°C accelerates the process. The x-ray pattern for the decomposed sample is shown in Fig. 20b, and the peak intensity is significantly degraded compared to the “fresh” sample despite taking a much longer 7-hour scan.

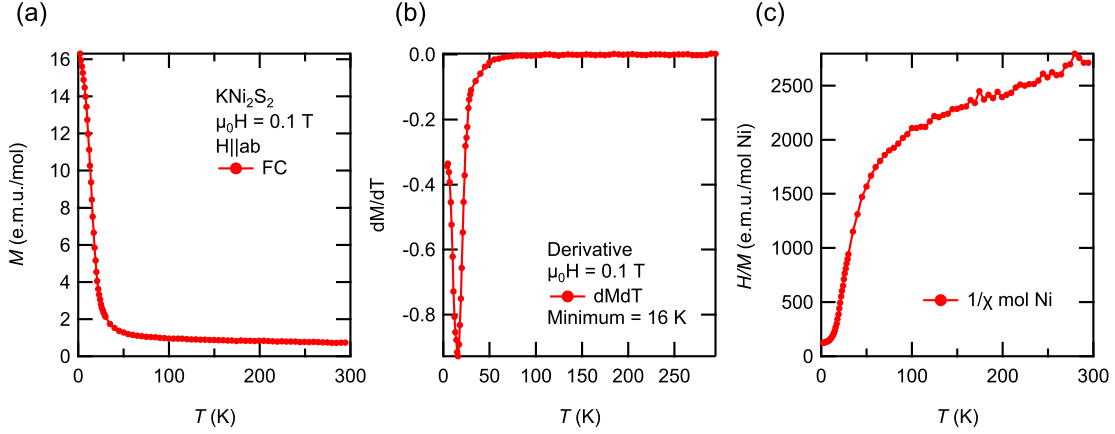


FIG. 21. (a) M v. T for a KNi_2S_2 single crystal. (b) While it is difficult to tell from the magnetization curve whether the compound is ferromagnetic or paramagnetic, plotting the derivative shows a distinct minimum at 16 K. This minimum is seen in ferromagnets as pure paramagnets do not have this minimum, but more work needs to be done to determine whether this compound truly is ferromagnetic. (c) By plotting H/M v. T , we see that this sample does not follow the Curie-Weiss law, or the modified Curie-Weiss law when $H \parallel ab$.

3. Magnetization Data

I present the results of my magnetization measurements on KNi_2S_2 in Fig. 21. Magnetization was measured previously on polycrystalline samples [38]. In this previous work, they measure a linear, nearly temperature-independent magnetization that they claim to be the result of a Ni impurity. Ni has $T_C = 628$ K, which could explain their magnetization measurement. In our measurement, however, we see a significant increase in M below 25 K. Furthermore, by taking the temperature derivative of this curve (Fig. 21b), we find a clear local minimum at $T = 16$ K, which would not exist if KNi_2S_2 was purely paramagnetic. This local minimum is 10 K below what we observed in KNi_4S_2 , so it is unlikely that it is due to a 142 phase impurity. Furthermore, we find an unusual shape of the H/M v. T curve when $H \parallel ab$, as shown in Fig. 21c, that does not follow the Curie-Weiss law, or the modified Curie-Weiss law. There are examples, however, of compounds with a unconventional H/M v. T curve along one axis, while following the Curie-Weiss law along a different crystal axis, such as the Kondo-lattice ferromagnet CeAgSb_2 [39]. It is possible that the magnetic features in KNi_2S_2 are anisotropic, and therefore obscured in studies using polycrystalline samples. $H \parallel c$ could be measured to confirm this hypothesis.

C. $K_2Ni_3S_4$

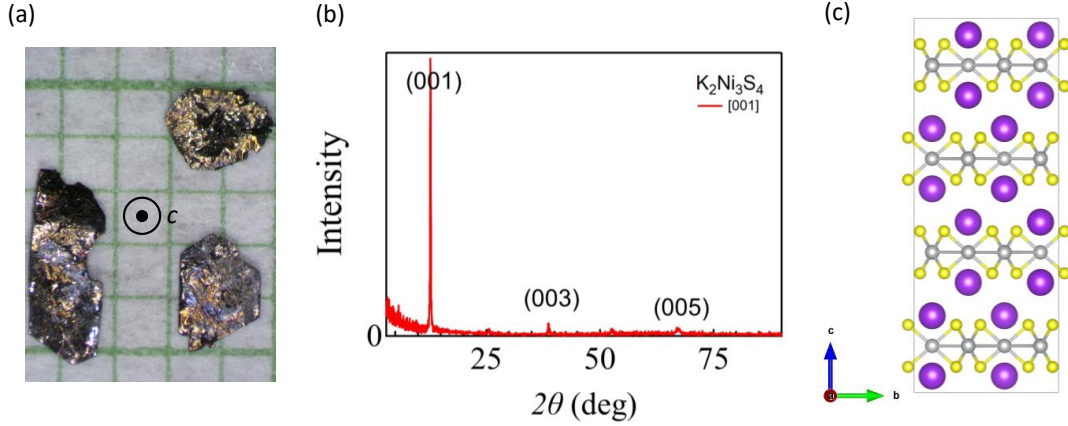


FIG. 22. (a) $K_2Ni_3S_4$ single crystals photographed on mm-grid paper. The 234 phase has a hexagonal crystal structure, and the c axis points out of the page. (b) The PXRD data shows peaks associated with the c axis, which is consistent with measuring a single crystal in this orientation. (c) The crystal structure of the 234 phase, Hexagonal with the $Fddd$ space group.

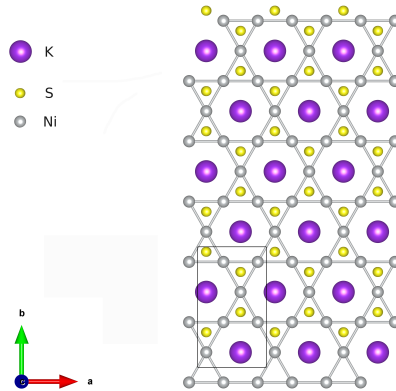


FIG. 23. $K_2Ni_3S_4$ crystal structure as viewed along the c axis to highlight its kagome lattice. Thank you to Max Wright for the help making this figure.

1. Introduction

$K_2Ni_3S_4$ has not been extensively studied. Initial reports suggested that $K_2Ni_3S_4$ might be paramagnetic [40, 41], however, further investigation was inconclusive given the small size of the magnetic moment and the potential presence of a ferromagnetic

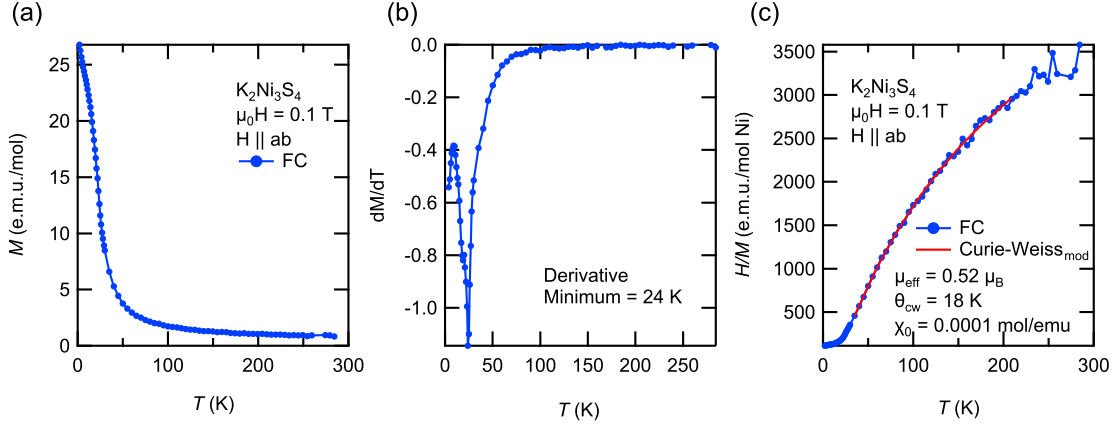


FIG. 24. (a) M v. T for a $\text{K}_2\text{Ni}_3\text{S}_4$ single crystal. (b) Taking the temperature derivative of the magnetization is puzzling. On one hand, there is a clear minimum at 24 K which is similar to the T_C we measure for the 142 phase. On the other hand, there is a local maximum followed by a downturn at low temperatures, which suggests the presence of paramagnetism. Clearly, more research needs to be done on the magnetism of the 234 phase. (c) It is possible to fit the high temperature portion of the H/M v. T plot to a modified Curie-Weiss function.

impurity due to Ni [42]. The existing data on its physical properties suggest it is a semiconductor showing resistivity increases as temperature decreases [42].

Elder et al. were the first to use single crystal x-ray diffraction to determine the crystal structure and found that it forms a honeycomb lattice ($Fddd$ space group) [42]. In Zhou's work the presence of an alpha and beta structural phase was discovered in the material [21]. By combining these two ideas, we can explore the structural and magnetic properties of this phase using the same synthetic method and use of chemical substitution. Kuki et al. have already demonstrated this is possible by complete substitution of the potassium site with rubidium. $\text{Rb}_2\text{Ni}_3\text{S}_4$ arranges in a kagome lattice and exhibited weak ferromagnetic features at low temperatures, which is interesting since the electronic structure of nickel is $3d^8$, and traditionally Ni^{2+} is diamagnetic [43].

The $\text{K}_2\text{Ni}_3\text{S}_4$ phase crystals are shown in Fig. 22a. They have a hexagonal crystal structure and grow much larger than the 142 phase since they are the thermodynamically stable product. These crystals have previously been synthesized with a flux-growth method starting with Ni and K_2S powders [42].

While a previous report mentioned that the 234 phase is either a weak paramagnet, or even potentially diamagnetic with any magnetism being due to a ferromagnetic impurity, they did not show their magnetization data. Our measurements of M v. T

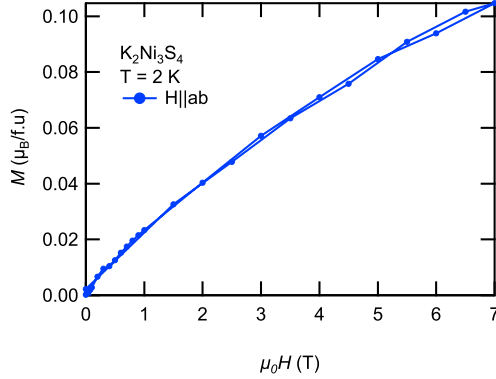


FIG. 25. M v. H at $T = 2$ K for a $K_2Ni_3S_4$ single crystal.

can be found in Fig. 24 and the M v. H can be found in Fig. 25. Our data suggests that the presence of paramagnetism, though some anomalies present themselves that would warrant further exploration.

2. Magnetization Data

Although preliminary measurements down to $T = 2$ K did not yield any great discoveries, we can use this information and our ability to synthesize large single crystal samples to explore the intermediate doping and monitor the changes in the kagome lattice and magnetic properties. The transition metal site also changes the properties as well since $Rb_2Pt_3S_4$ was found to have even stronger magnetic ordering. The possibility of substituting the alkali metal with an alkaline earth metal has yet to be explored and such a substitution has shown interesting results in other compounds, as discussed in the following section. In summary, this system, much like the other nickel sulfide phases explored in this thesis, gives us a rich platform to study novel magnetic properties.

V. FUTURE WORK

A. Potential Dopings

Further exploration of this rediscovered synthetic method for single crystal growth could reveal a large number of new materials to study. Zhou et al. have already used this method to synthesize over 30 previously unreported compounds in a relatively

short amount of time [44]. The variety of potential precursors are not limited to the Alkali/Alkaline Earth: Transition Metal: chalcogenide formula. Even rare earth oxides are viable as seen in previous literature [45, 46], furthering the myriad of possible compounds to include rare earth nickelates [47].

The nickel sulfides synthesized in this project are also good candidates to monitor the effects of doping on the ferromagnetism in the 142 phase and superconductivity in the 122 phase. Doping can be possible on the alkali site using an alkaline earth metal hydroxide such as $\text{Ba}(\text{OH})_2$, $\text{Ca}(\text{OH})_2$, or $\text{Cu}(\text{OH})_2$ to substitute on the nickel site. We see that KCu_2S_2 is a naturally occurring complex known as Murunskite and barium substitution studies have been done on the potassium site giving us confidence that our hypothesized dopants should insert themselves in the lattice [48, 49].

We can also measure the physical properties down to 0.35 K with our ^3He probe in the PPMS which would allow us to see our expected superconducting transition at 0.46 K in the 122 phase, and follow the transition after doping. Using our synthesis procedure, we were able to grow samples with a nominal 20% doping of Cu on the Ni site in the 142 phase. From our preliminary data, we saw little shift in the XRD, but we did see a lower transition temperature in magnetization data along with a smaller hysteresis loop which is encouraging with suppressing the ferromagnetic state in mind. Though more experimental synthesis are promising.

B. Pressure Studies

Since we have evidence for weak ferromagnetism in KNi_4S_2 , a question we can ask is what will happen to the FM state if we apply pressure? Itinerant ferromagnets have a history of interesting physics occurring under pressure, whether it be the emergence of superconductivity in UGe_2 [50, 51] near its Quantum Critical Point (QCP), ferromagnetic to antiferromagnetic ordering seen in LaCrGe_3 [52–54], or quantum tricriticality in CeTiGe_3 [55]. Exploring the $T - p - H$ magnetic phase diagram of our KNi_4S_2 system may yield new insight into the behavior of these weakly itinerant ferromagnetic systems. This compound is well-suited for collaborations with other labs that specialize in high pressure studies in condensed matter materials.

VI. CONCLUSION

Single crystals of KNi_4S_2 have been synthesized using a molten hydroxide flux growth. They have been characterized using XRD and the axes have been determined. Our magnetization data suggests the 142 phase is ferromagnetic ($T_C \approx 25$ K). Anisotropic single crystal measurements show similar properties along a and c and suggest that the b axis is the easy magnetization direction. Superconducting KNi_2S_2 was synthesized by simply changing the temperature profile, XRD and magnetization data was taken from 300 K down to 2 K and no phase transition was observed. We also synthesized the largest reported single crystals of $\text{K}_2\text{Ni}_3\text{S}_4$, however, magnetization data showed no phase transition down to 2 K. Hydroxide-melt synthesis could be a very lucrative synthesis for our lab to explore, the precursors are inexpensive, environmentally friendlier than those traditionally used in solid-state, and can open up a new realm of kinetically stable products in our exploration for superconductivity and magnetism.

ACKNOWLEDGMENTS

I would like to first thank my advisor Dr. Valentin Taufour for all his patience and guidance through the ups and downs of graduate school. I am also grateful for my fellow group members: Rahim Ullah for his help in writing this thesis, his help with the MPMS and for him being a true friend throughout my time here. Hanshang Jin, Yunshu Shi and Zihao Shen, for their help teaching me the PPMS and for dealing with my many temper tantrums when I snapped my crystals, and of course Peter Klavins for all of his help in teaching me the various instruments. This group truly made me feel welcome, even as a chemist among physicists. I would not have made it this far without them. Lastly, I would like to thank my family for their constant love, encouragement and support, especially my mother and father, Cecilie and Ben Quezada, for always being in my corner, I love you mom and dad. I would also like to thank my dear partner, Linzee Faulkner, for her incredible understanding and help keeping me together through everything that's been thrown at us, you have done more than I ever could have asked for and I love you more and more for it. Finally, this thesis is dedicated to my son Frankie, he is my biggest blessing, my strongest motivation and kept me going even when I didn't think I had anything left. I couldn't have done it without you, son.

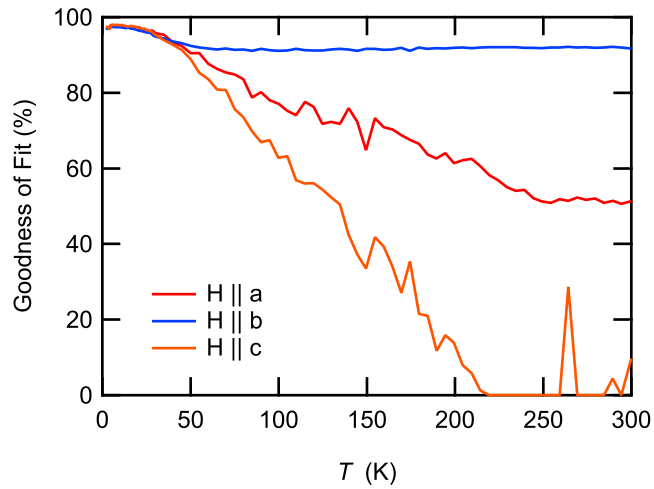


FIG. 26. The goodness of fit as reported by the MPMS of the KNi_4S_2 single crystal mosaic along the a , b , and c axis. Surprisingly, the b axis fit is much better than the a and c axes, yet results in a background magnetization.

Appendix A: Table of Synthesis Notes

The following pages detail my optimization of the KNi_4S_2 synthesis via salt-melt synthesis.

Appendix B: MPMS Goodness of Fit

Batch	Stoichiometry	Scale	Temperature Profile	Results
EC	LiOH:KOH	Ni(OH) ₂ amount	RR:DTemp:DTime:CR	Notes
EC443	0.3:0.7	1.159g	180°C/hr:450°C:30hr:10°C/hr	Black Powder (BP)
EC444	0.3:0.7	1.159g	180°C/hr:450°C:30Hr:6°C/hr	BP
EC445	0.3:0.7	0.5793g	180°C/hr:450°C:30Hr:5°C/hr	BP
EC456	0.3:0.7	0.5785g	180°C/hr:450°C:30Hr:6°C/hr	BP
EC458	0.54:0.46	0.7505g	98.75°C/hr:450°C:30Hr:5°C/hr	BP
EC458b	0.54:0.46	0.7512g	98.75°C/hr:425°C:30Hr:5°C/hr	BP
EC458c	0.54:0.46	0.7506g	98.75°C/hr:425°C:30Hr:5°C/hr	BP
EC458c			Started Grinding KOH	
EC461	0.54:0.46	0.7509g	900°C/hr:450°C:30Hr:5°C/hr	BP and “shiny” small crystals
EC461b	0.54:0.46	0.7507g	900°C/hr:450°C:30Hr:5°C/hr	BP and small “shiny” crystals
EC461b			Started drying sulfur before rxn	
EC461c	0.54:0.46	0.7507g	900°C/hr:450°C:30Hr:5°C/hr	small hexagonal crystals
EC461c			tried capping the crucible	small 234 phase
EC472	0.54:0.46	0.7514g	900°C/hr:450°C:30Hr:4°C/hr	BP and small “shiny” crystals
EC476	0.66:0.34	0.7455g	900°C/hr:450°C:30Hr:4°C/hr	BP
EC477	0.3:0.7	0.1012g	900°C/hr:450°C:30Hr:4°C/hr	BP and small 142
EC477			Zhou’s original stoichiometric ratio scaled down	

TABLE I. This table lists of all of the parameter changes and results throughout the different batches.

Batch	Stoichiometry Scale	Temperature Profile	Results
EC	LiOH:KOH	RR:DTemp:DTime:CR	Notes
EC477b	0.3:0.7	900°C/hr:450°C:30Hr:4°C/hr	BP
EC477b	0.0518g	too small of a batch, no crystals nucleated	
EC479	0.3:0.7	900°C/hr:450°C:30Hr:4°C/hr	larger 142 needles than EC477
EC485	0.3:0.7	900°C/hr:450°C:30Hr:4°C/hr	BP and small 142 needles
EC485	0.20271g	Changed to conical for better results	
EC491	0.3:0.7	900°C/hr:450°C:30Hr:4°C/hr	Larger 142 needles than EC479
EC491b	0.3:0.7	900°C/hr:450°C:30Hr:4°C/hr	same yield
EC493	0.3:0.7	900°C/hr:450°C:30Hr:Quench	Large 122 Crystals
EC493b	0.3:0.7	900°C/hr:450°C:30Hr:1°C/hr	Large 234 Crystals
EC503	0.3:0.7	900°C/hr:450°C:30Hr:2°C/hr	Large 234 Crystals
EC507	0.3:0.7	900°C/hr:450°C:30Hr:3°C/hr	Large 234 Crystals
EC512	0.3:0.7	900°C/hr:450°C:25Hr:Quench	Large 122 Crystals
EC513	0.3:0.7	600°C/hr:300°C:10Hr warm to 450°C:25Hr:Quench	Largest 142 Crystals so far
EC518	0.3:0.7	600°C/hr:300°C:10Hr warm to 450°C:25Hr:Quench	Largest 142 Crystals so far
EC518b	0.3:0.7	600°C/hr:300°C:10Hr warm to 450°C/Quench	Largest 142 Crystals
EC518b		This recipe was used with subtle changes onwards	

TABLE II. This table lists of all of the parameter changes and results throughout the different batches.

-
- [1] H. K. Onnes, Further experiments with liquid helium. on the change of electric resistance of pure metals at very low temperatures etc. the resistance of pure mercury at helium temperatures, Koninklijke Nederlandsche Akademie van Wetenschappen **13**, 1274 (1910).
- [2] R. Combescot, *Superconductivity* (Cambridge University Press, 2022).
- [3] J. Bardeen, L. N. Cooper, and J. R. Schrieffer, Theory of superconductivity, Phys. Rev. **108**, 1175 (1957).
- [4] J. G. Bednorz and K. A. Muller, Possible high T_c superconductivity in the BaLaCuO system, Zeitschrift fur Physik B Condensed Matter **64**, 189 (1986).
- [5] B. Batlogg, R. J. Cava, L. W. Rupp, A. M. Mujsce, J. J. Krajewski, J. P. Remeika, W. F. Peck, A. S. Cooper, and G. P. Espinosa, Density of states and isotope effect in BiO superconductors: Evidence for nonphonon mechanism, Phys. Rev. Lett. **61**, 1670 (1988).
- [6] T. Palstra, O. Zhou, Y. Iwasa, P. Sulewski, R. Fleming, and B. Zegarski, Superconductivity at 40K in cesium doped C60, Solid State Communications **93**, 327 (1995).
- [7] C. B. Eom, M. K. Lee, J. H. Choi, L. J. Belenky, X. Song, L. D. Cooley, M. T. Naus, S. Patnaik, J. Jiang, M. Rikel, A. Polyanskii, A. Gurevich, X. Y. Cai, S. D. Bu, S. E. Babcock, E. E. Hellstrom, D. C. Larbalestier, N. Rogado, K. A. Regan, M. A. Hayward, T. He, J. S. Slusky, K. Inumaru, M. K. Haas, and R. J. Cava, High critical current density and enhanced irreversibility field in superconducting MgB₂ thin films, Nature **411**, 558 (2001).
- [8] Y. Kamihara, H. Hiramatsu, M. Hirano, R. Kawamura, H. Yanagi, T. Kamiya, and H. Hosono, Iron-based layered superconductor: LaOFeP, Journal of the American Chemical Society **128**, 10012 (2006).
- [9] Z.-A. Ren, G.-C. Che, X.-L. Dong, J. Yang, W. Lu, W. Yi, X.-L. Shen, Z.-C. Li, L.-L. Sun, F. Zhou, and Z.-X. Zhao, Superconductivity and phase diagram in iron-based arsenic-oxides ReFeAsO_{1- δ} (Re = rare-earth metal) without fluorine doping, Europhysics Letters **83**, 17002 (2008).
- [10] A. P. Drozdov, M. I. Erements, I. A. Troyan, V. Ksenofontov, and S. I. Shylin, Conventional superconductivity at 203 kelvin at high pressures in the sulfur hydride system,

- Nature **525**, 73 (2015).
- [11] A. P. Drozdov, P. P. Kong, V. S. Minkov, S. P. Besedin, M. A. Kuzovnikov, S. Mozaffari, L. Balicas, F. F. Balakirev, D. E. Graf, V. B. Prakapenka, E. Greenberg, D. A. Knyazev, M. Tkacz, and M. I. Erements, Superconductivity at 250 K in lanthanum hydride under high pressures, Nature **569**, 528 (2019).
- [12] F. Cellani, L. Liberatori, A. Saggese, R. Messi, S. Pace, and N. Sparvieri, *Ozone annealing of YBCO superconductors*, Tech. Rep. (Istituto Nazionale di Fisica Nucleare, Italy, 1988) iNFN-LNF-88-71(P).
- [13] M. R. Koblishka, A. Koblishka-Veneva, S. P. K. Naik, D. Gokhfeld, and M. Murakami, Porous high- T_c superconducting cuprates: Advantages and applications, Journal of Physics: Conference Series **1293**, 012009 (2019).
- [14] A. S. Botana and M. R. Norman, Similarities and differences between LaNiO_2 and CaCuO_2 and implications for superconductivity, Phys. Rev. X **10**, 011024 (2020).
- [15] A. S. Botana, K.-W. Lee, M. R. Norman, V. Pardo, and W. E. Pickett, Low valence nickelates: Launching the nickel age of superconductivity, Frontiers in Physics **9**, 10.3389/fphy.2021.813532 (2022).
- [16] D. Li, K. Lee, B. Y. Wang, M. Osada, S. Crossley, H. R. Lee, Y. Cui, Y. Hikita, and H. Y. Hwang, Superconductivity in an infinite-layer nickelate, Nature **572**, 624 (2019).
- [17] D. Li, B. Y. Wang, K. Lee, S. P. Harvey, M. Osada, B. H. Goodge, L. F. Kourkoutis, and H. Y. Hwang, Superconducting dome in $\text{Nd}_{1-x}\text{Sr}_x\text{NiO}_2$ infinite layer films, Phys. Rev. Lett. **125**, 027001 (2020).
- [18] M.-Y. Choi, K.-W. Lee, and W. E. Pickett, Role of $4f$ states in infinite-layer NdNiO_2 , Phys. Rev. B **101**, 020503 (2020).
- [19] H. Sakakibara, H. Usui, K. Suzuki, T. Kotani, H. Aoki, and K. Kuroki, Model construction and a possibility of cupratelike pairing in a new d^9 nickelate superconductor $(\text{Nd,Sr})\text{NiO}_2$, Phys. Rev. Lett. **125**, 077003 (2020).
- [20] B.-X. Wang, H. Zheng, E. Kriviyakina, O. Chmaissem, P. P. Lopes, J. W. Lynn, L. C. Gallington, Y. Ren, S. Rosenkranz, J. F. Mitchell, and D. Phelan, Synthesis and characterization of bulk $\text{Nd}_{1-x}\text{Sr}_x\text{NiO}_2$ and $\text{Nd}_{1-x}\text{Sr}_x\text{NiO}_3$, Phys. Rev. Mater. **4**, 084409 (2020).

- [21] X. Zhou, D. J. Mandia, H. Park, M. Balasubramanian, L. Yu, J. Wen, A. Yakovenko, D. Y. Chung, and M. G. Kanatzidis, New compounds and phase selection of nickel sulfides via oxidation state control in molten hydroxides, *Journal of the American Chemical Society* **143**, 13646 (2021), PMID: 34410691, <https://doi.org/10.1021/jacs.1c05107>.
- [22] M. Jiang, M. Berciu, and G. A. Sawatzky, Critical nature of the ni spin state in doped NdNiO₂, *Phys. Rev. Lett.* **124**, 207004 (2020).
- [23] M. Xiao, B. Luo, M. Konarova, Z. Wang, and L. Wang, Molten salt synthesis of atomic heterogeneous catalysts: Old chemistry for advanced materials, *European Journal of Inorganic Chemistry* **2020**, 2942 (2020), <https://chemistry-europe.onlinelibrary.wiley.com/doi/pdf/10.1002/ejic.202000391>.
- [24] W. Sundermeyer, Fused salts and their use as reaction media, *Angewandte Chemie International Edition in English* **4**, 222 (1965), <https://onlinelibrary.wiley.com/doi/pdf/10.1002/anie.196502221>.
- [25] J. Boltersdorf, N. King, and P. A. Maggard, Flux-mediated crystal growth of metal oxides: synthetic tunability of particle morphologies, sizes, and surface features for photocatalysis research, *CrystEngComm* **17**, 2225 (2015).
- [26] X. Liu, N. Fechner, and M. Antonietti, Salt melt synthesis of ceramics, semiconductors and carbon nanostructures, *Chem. Soc. Rev.* **42**, 8237 (2013).
- [27] H. Lux, "säuren" und "basen" im schmelzfluss: Die bestimmung der sauerstoffionenkonzentration, *Zeitschrift für Elektrochemie und angewandte physikalische Chemie* **45**, 303 (1939), <https://onlinelibrary.wiley.com/doi/pdf/10.1002/bbpc.19390450405>.
- [28] H. Flood and T. Forland, The acidic and basic properties of oxides, *Acta Chem Scand* **1**, 592 (1947).
- [29] X. Zhou, B. Wilfong, X. Chen, C. Laing, I. R. Pandey, Y.-P. Chen, Y.-S. Chen, D.-Y. Chung, and M. G. Kanatzidis, Sr(Ag_{1-x}Li_x)₂Se₂ and [Sr₃Se₂][(Ag_{1-x}Li_x)₂Se₂] tunable direct band gap semiconductors, *Angewandte Chemie International Edition* **62**, e202301191 (2023), <https://onlinelibrary.wiley.com/doi/pdf/10.1002/anie.202301191>.
- [30] C. W. Bale and A. D. Pelton, Coupled phase diagram and thermodynamic analysis of the 18 binary systems formed among Li₂CO₃, K₂CO₃, Na₂CO₃, LiOH, KOH, NaOH, Li₂SO₄, K₂SO₄ and Na₂SO₄, *Calphad* **6**, 255 (1982).

- [31] S. Walspurger, L. Boels, P. Cobden, G. Elzinga, W. Haije, and R. vanden Brink, The crucial role of the k^+ -aluminium oxide interaction in k^+ -promoted alumina- and hydrotalcite-based materials for CO_2 sorption at high temperatures, *ChemSusChem* **1**, 643 (2008), <https://chemistry-europe.onlinelibrary.wiley.com/doi/pdf/10.1002/cssc.200800085>.
- [32] M. McElfresh, *Fundamentals of Magnetism and Magnetic Measurements Featuring Quantum Design's Magnetic Property Measurement System* (Quantum Design, 1994).
- [33] E. A. Yelland, S. J. C. Yates, O. Taylor, A. Griffiths, S. M. Hayden, and A. Carrington, Ferromagnetic properties of ZrZn_2 , *Phys. Rev. B* **72**, 184436 (2005).
- [34] E. Granado, H. Martinho, M. S. Sercheli, P. G. Pagliuso, D. D. Jackson, M. Torelli, J. W. Lynn, C. Rettori, Z. Fisk, and S. B. Oseroff, Unconventional metallic magnetism in LaCrSb_3 , *Physical Review Letters* **89**, 10.1103/physrevlett.89.107204 (2002).
- [35] X. Lin, V. Taufour, S. L. Bud'ko, and P. C. Canfield, Suppression of ferromagnetism in the $\text{La}(\text{V}_x\text{Cr}_{1-x})\text{Sb}_3$ system, *Philosophical Magazine* **94**, 1277 (2013).
- [36] Y. Liu, M. A. Tanatar, V. G. Kogan, H. Kim, T. A. Lograsso, and R. Prozorov, Upper critical field of high-quality single crystals of KFe_2As_2 , *Phys. Rev. B* **87**, 134513 (2013).
- [37] V. Taufour, N. Foroozani, M. A. Tanatar, J. Lim, U. Kaluarachchi, S. K. Kim, Y. Liu, T. A. Lograsso, V. G. Kogan, R. Prozorov, S. L. Bud'ko, J. S. Schilling, and P. C. Canfield, Upper critical field of KFe_2As_2 under pressure: A test for the change in the superconducting gap structure, *Physical Review B* **89**, 10.1103/physrevb.89.220509 (2014).
- [38] J. R. Neilson, T. M. McQueen, A. Llobet, J. Wen, and M. R. Suchomel, Charge density wave fluctuations, heavy electrons, and superconductivity in KNi_2S_2 , *Phys. Rev. B* **87**, 045124 (2013).
- [39] S. E. Nikitin, A. Podlesnyak, J. Xu, D. Voneshen, M. D. Le, S. L. Bud'ko, P. C. Canfield, and D. A. Sokolov, Magnetic field induced softening of spin waves and hard-axis order in the kondo-lattice ferromagnet CeAgSb_2 , *Physical Review B* **104**, 115169 (2021).
- [40] W. Bronger, J. Eyck, W. Rüdorff, and A. Stöussel, Über thio- und selenonickolate und -palladate der schweren alkalimetalle, *Zeitschrift für anorganische und allgemeine Chemie* **375**, 1 (1970), <https://onlinelibrary.wiley.com/doi/pdf/10.1002/zaac.19703750102>.
- [41] W. Bronger, R. Rennau, and D. Schmitz, Schichtstrukturen ternärer chalcogenide $\text{A}_2\text{M}_3\text{X}_4$ ($\text{A} = \text{K}, \text{Rb}, \text{Cs}$; $\text{M} = \text{Ni}, \text{Pd}, \text{Pt}$; $\text{X} = \text{S}, \text{Se}$), *Zeitschrift für anorganische*

- und allgemeine Chemie **597**, 27 (1991).
- [42] S. H. Elder, S. Jovic, R. Brec, M. Gelibert, and F. J. DiSalvo, Structural and electronic properties of $K_2Ni_3S_4$, a pseudo-two dimensional compound with a honeycomb-like arrangement, *Journal of Alloys and Compounds* **235**, 135 (1996).
- [43] R. Kuki, Y. Fujiwara, T. Ono, K. Iio, M. Tachibana, T. Atake, and Y. Nakai, Dilute kagomé lattice magnetism with $S = 1/2$ on $Rb_2(Pd_{1-x}M_x)_3S_4$ ($M = Co, Mn$), *Progress of Theoretical Physics Supplement* **159**, 61 (2005), <https://academic.oup.com/ptps/article-pdf/doi/10.1143/PTPS.159.61/5294814/159-61.pdf>.
- [44] X. Zhou, V. S. C. Kolluru, W. Xu, L. Wang, T. Chang, Y.-S. Chen, L. Yu, J. Wen, M. K. Y. Chan, D. Y. Chung, and M. G. Kanatzidis, Discovery of chalcogenides structures and compositions using mixed fluxes, *Nature* **612**, 72 (2022).
- [45] R. Hinterding, Z. Zhao, C. Zhang, and A. Feldhoff, Anisotropic growth of $La_2NiO_{4+\delta}$: Influential pre-treatment in molten-flux synthesis, *Journal of Crystal Growth* **523**, 125135 (2019).
- [46] J. L. Luce and A. M. Stacy, Crystallization of $LnCu_2O_4$ ($Ln = La, Nd, Sm, Eu, Gd, Dy, Ho, Y, Er$) from hydroxide melts: synthesis and structure, *Chemistry of Materials* **9**, 1508 (1997).
- [47] S. I. Arockiam, L. J. Berchmans, S. Angappan, A. Visuvasam, and V. Mani, Synthesis of lanthanum nickelate and praseodymium substituted compounds by molten salt technique, *Materials Science Forum* **699**, 67 (2012).
- [48] I. V. Pekov, N. V. Zubkova, D. V. Lisitsyn, and D. Y. Pushcharovsky, Crystal chemistry of murunskite, *Doklady Earth Sciences* **424**, 139 (2009).
- [49] X. Zhang, T. Hogan, C. R. Kannewurf, and M. G. Kanatzidis, Sulfur p-band hole generation in β - $BaCu_2S_2$. synthesis of metallic $K_xBa_{1-x}Cu_2S_2$ from molten mixed K-Ba polysulfide salts, *Journal of Alloys and Compounds* **236**, 1 (1996).
- [50] C. Pfleiderer and A. D. Huxley, Pressure dependence of the magnetization in the ferromagnetic superconductor UGe_2 , *Physical Review Letters* **89**, 147005 (2002).
- [51] V. Taufour, D. Aoki, G. Knebel, and J. Flouquet, Tricritical point and wing structure in the itinerant ferromagnet UGe_2 , *Physical Review Letters* **105**, 10.1103/physrevlett.105.217201 (2010).

- [52] V. Taufour, U. S. Kaluarachchi, R. Khasanov, M. C. Nguyen, Z. Guguchia, P. K. Biswas, P. Bonfà, R. D. Renzi, X. Lin, S. K. Kim, E. D. Mun, H. Kim, Y. Furukawa, C.-Z. Wang, K.-M. Ho, S. L. Bud'ko, and P. C. Canfield, Ferromagnetic quantum critical point avoided by the appearance of another magnetic phase in LaCrGe_3 under pressure, *Physical Review Letters* **117**, 10.1103/physrevlett.117.037207 (2016).
- [53] U. S. Kaluarachchi, S. L. Bud'ko, P. C. Canfield, and V. Taufour, Tricritical wings and modulated magnetic phases in LaCrGe_3 under pressure, *Nature Communications* **8**, 10.1038/s41467-017-00699-x (2017).
- [54] X. Lin, V. Taufour, S. L. Bud'ko, and P. C. Canfield, Suppression of ferromagnetism in the $\text{LaV}_x\text{Cr}_{1-x}\text{Ge}_3$ system, *Phys. Rev. B* **88**, 094405 (2013).
- [55] U. S. Kaluarachchi, V. Taufour, S. L. Bud'ko, and P. C. Canfield, Quantum tricritical point in the temperature-pressure-magnetic field phase diagram of CeTiGe_3 , *Physical Review B* **97**, 10.1103/physrevb.97.045139 (2018).